nature COMMUNICATIONS

ARTICLE

Received 21 Mar 2013 | Accepted 13 Jun 2013 | Published 15 Jul 2013

DOI: 10.1038/ncomms3148

Turbulence drives microscale patches of motile phytoplankton

William M. Durham[1,2], Eric Climent[3], Michael Barry[1], Filippo De Lillo[4,5], Guido Boffetta[5],
Massimo Cencini[6] & Roman Stocker[1]

Patchiness plays a fundamental role in phytoplankton ecology by dictating the rate at which individual cells encounter each other and their predators. The distribution of motile phytoplankton species is often considerably more patchy than that of non-motile species at submetre length scales, yet the mechanism generating this patchiness has remained unknown. Here we show that strong patchiness at small scales occurs when motile phytoplankton are exposed to turbulent flow. We demonstrate experimentally that *Heterosigma akashiwo* forms striking patches within individual vortices and prove with a mathematical model that this patchiness results from the coupling between motility and shear. When implemented within a direct numerical simulation of turbulence, the model reveals that cell motility can prevail over turbulent dispersion to create strong fractal patchiness, where local phytoplankton concentrations are increased more than 10-fold. This 'unmixing' mechanism likely enhances ecological interactions in the plankton and offers mechanistic insights into how turbulence intensity impacts ecosystem productivity.

---

[1] Ralph M. Parsons Laboratory, Department of Civil and Environmental Engineering, Massachusetts Institute of Technology, 77 Massachusetts Avenue, Cambridge, Massachusetts 02139, USA. [2] Department of Zoology, University of Oxford, South Parks Road, Oxford OX1 3PS, UK. [3] Institut de Mécanique des Fluides, Université de Toulouse, INPT-UPS-CNRS, Allée du Pr. Camille Soula, F-31400 Toulouse, France. [4] DICCA, Università di Genova, via Montallegro 1, Genova 16145, Italy. [5] Dipartimento di Fisica and INFN, Università di Torino, via P. Giuria 1, Torino 10125, Italy. [6] Istituto dei Sistemi Complessi, Consiglio Nazionale delle Ricerche, via dei Taurini 19, Rome 00185, Italy. Correspondence and requests for materials should be addressed to W.M.D. (email: william.durham@zoo.ox.ac.uk) or to R.S. (email: romans@mit.edu).

Patchiness in the distribution of phytoplankton has long intrigued fishermen and scientists alike, because it generates hotspots of organisms at higher trophic levels[1,2] and modulates species diversity[3], rates of fish recruitment[4] and population stability[5]. While phytoplankton patchiness at large spatial scales is driven by reproduction, growth is too slow to generate structure at scales $\lesssim 1$ km vis-à-vis the homogenizing effect of turbulence[6,7]. Below this bottleneck scale, patchiness generated by locally enhanced growth is transferred to progressively smaller scales by turbulent stirring.

Whereas traditional plankton sampling techniques that utilize nets and bottles average over scales of metres, new technologies, including high-resolution fluorometers[8,9], underwater imaging[10,11] and syringe arrays[12], offer vastly improved resolution of plankton distributions, and have revealed that the microscale ($\sim$1–10 cm) distribution of motile phytoplankton species (for example, dinoflagellates) is often considerably more patchy than the distribution of non-motile species (for example, diatoms)[10–12]. However, the mechanisms that underlie this observation have remained elusive. Here we show that phytoplankton motility, when occurring in a turbulent flow, generates intense patchiness, far exceeding that of randomly distributed, non-motile populations.

Results

***H. akashiwo* motility within a steady vortex flow.** Following the tradition of using a vortical flow as a first proxy for small-scale turbulence[13], we exposed the motile, harmful algal bloom forming phytoplankter *H. akashiwo* to a steady vortex pair created via cavity flow (Fig. 1a,b; Methods). Video microscopy revealed that motile cells formed dense patches (Fig 1c, Supplementary Movie 1). In addition to swimming into downwelling regions, as previously predicted[14,15] and observed in pipe flow[16], they accumulated inside the vortices' cores, showing that individual vortices can trigger striking patches of motile phytoplankton. In contrast, killed cells remained randomly distributed (Supplementary Fig. S2), demonstrating that motility was an essential ingredient of patchiness.

Motility is a pervasive trait of phytoplankton. For example, 90% of species forming harmful algal blooms can swim[17]. Motility allows cells to reside near the surface during daylight hours to enhance light acquisition while accessing deeper waters with more nutrients and lower predation risk at night[18,19]. To migrate through the water column, many species rely on a stabilizing torque that biases their swimming in the vertical direction[20,21]. This stabilizing torque competes with the viscous torque exerted on cells by fluid shear (specifically, the spatial gradients in fluid velocity that contribute to vorticity), which acts to overturn cells. The resulting directed motility is termed gyrotaxis, and the gyrotactic reorientation timescale, B—the characteristic time a perturbed cell takes to return to its vertical equilibrium orientation, $\mathbf{k}$—provides a measure of how unstable the cell is to shear[20–22].

Gyrotactic motility within simulated flow fields. The hypothesis that the observed patchiness (Fig. 1c) originated from the coupling of motility and the shear in the vortical flow is strongly supported by a mathematical model of gyrotactic motility[21] (Methods). When parameterized with the measured swimming properties of *H. akashiwo*, this model yields cell distributions in close agreement with experiments (Fig. 1c,d; Supplementary

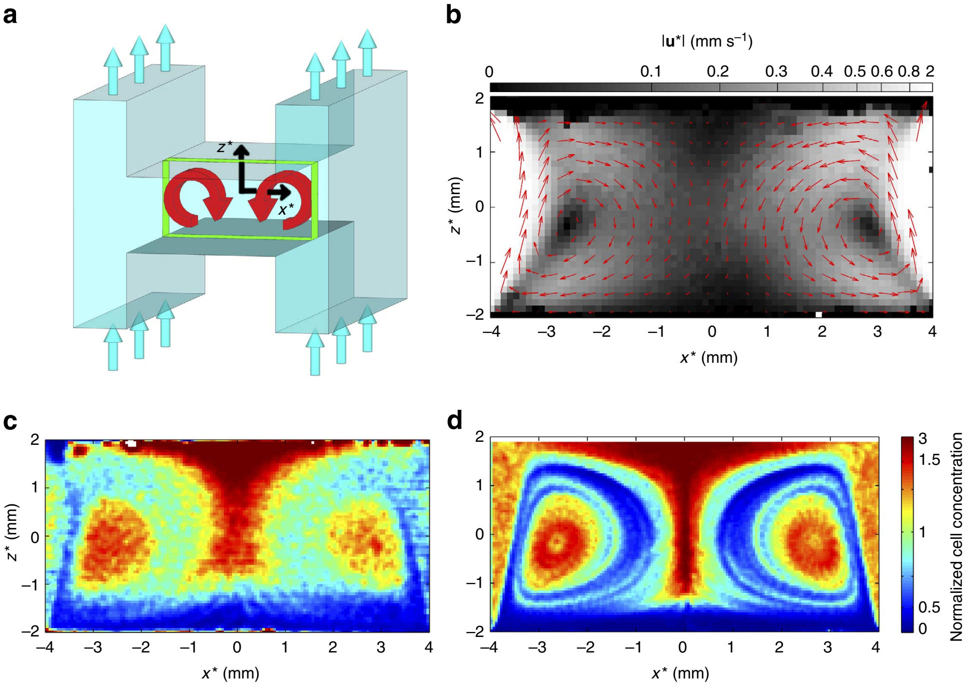

Figure 1 | Motility produces patchy phytoplankton distributions in a vortical flow. (**a**) An upward flow of a phytoplankton suspension (straight cyan arrows) past a central chamber was used to generate two counter-rotating vortices (curved red arrows). *H. akashiwo* cells, illuminated by a laser sheet, were imaged along the central plane (green rectangle). (**b**) The flow field $\mathbf{u}^*$ along the central plane of the chamber. Arrows denote fluid velocity and grey-scale intensity represents velocity magnitude. (**c**,**d**) Spatial distribution of phytoplankton cells in the central plane of the chamber from **c** experiments and **d** simulations. Cell concentrations were normalized by the mean concentration (Supplementary Methods). As *H. akashiwo* directs its motility opposite to gravity, cells that were able to escape the flow collected on the device's upper boundary: we thus used a nonlinear colourmap to simultaneously visualize these surface aggregations and those within the vortex cores. In a control experiment, killed cells remained randomly distributed (Supplementary Fig. S2). Asterisks denote dimensional variables and gravity acts in the $-z$ direction.

Fig. S4; Supplementary Movies 1 and 2). However, will patches of cells also occur in turbulent flow, where individual vortices are short-lived and the action of many vortices tends to disperse patchiness? To find out, we seeded a direct numerical simulation (DNS) of isotropic, homogeneous turbulence with up to 3.2×10^6 cells, whose motility was governed by the same model of gyrotaxis, and followed their trajectories until their spatial distribution reached a statistical steady state (Methods). We found that turbulence drives intense patchiness in the distribution of motile phytoplankton (Fig. 2b,c; Supplementary Movie 3), whereas non-motile cells follow the flow and remain randomly distributed (Fig. 2a).

While marine turbulence is comprised of fluid motion at many scales, phytoplankton cells (~1–100 μm) only experience

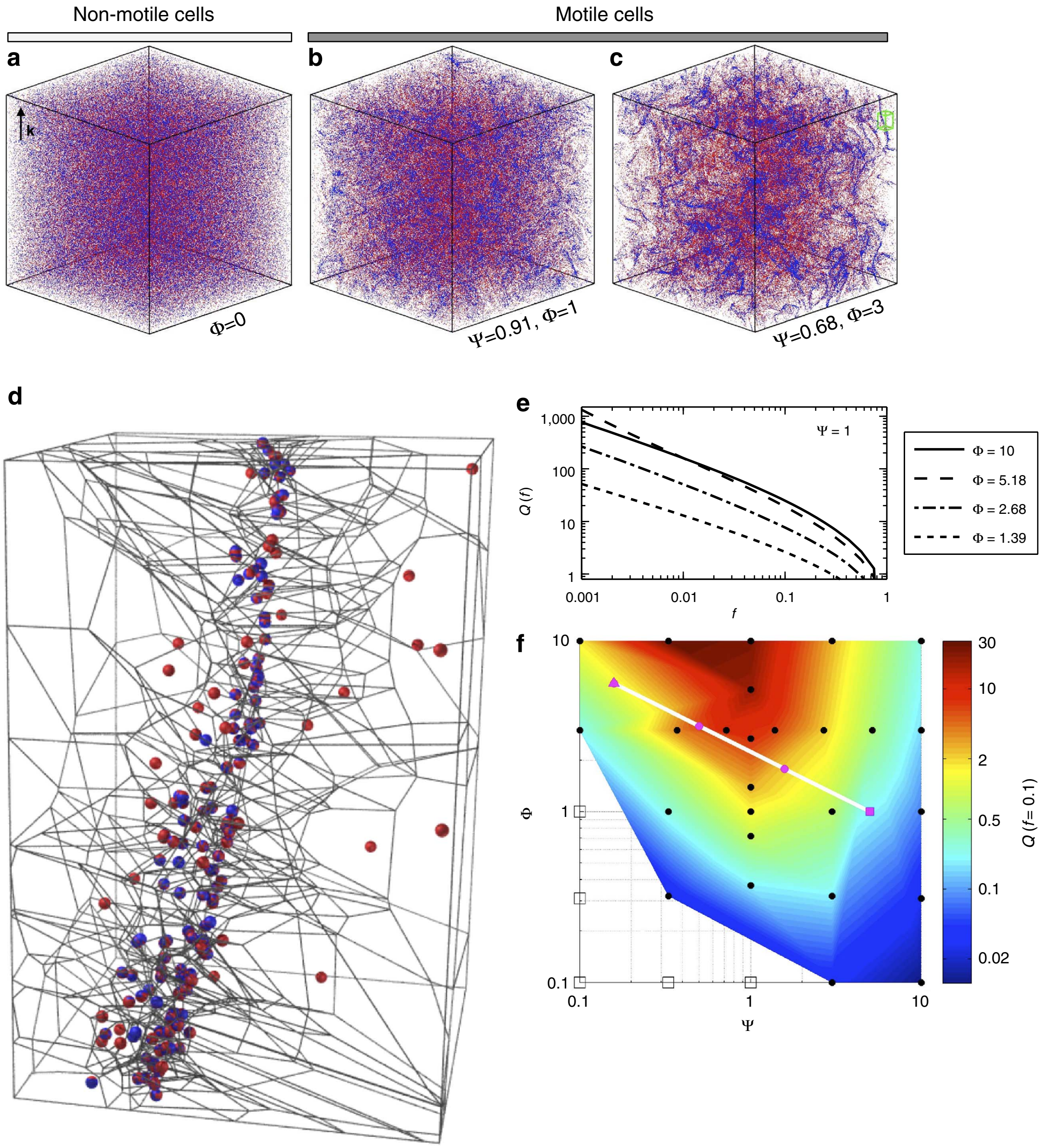

Figure 2 | Turbulence generates small-scale patchiness in the distribution of motile phytoplankton. (**a**–**c**) The positions of 300,000 cells swimming in a DNS of turbulent flow for three [Ψ, Φ] regimes. The 150,000 phytoplankton with the largest concentration (corresponding to $f = 0.5$) are shown in blue, the remaining cells in red. Motile cells (**b**,**c**) exhibit strong patchiness, whereas non-motile cells (**a**) remain randomly distributed. (**d**) Three-dimensional Voronoi tessellation used to calculate the local cell concentration. Each cell is assigned the polyhedron that includes all points whose distance to that cell is smaller than its distance to any other cell. The inverse of the polyhedron's volume is the cell concentration. The region shown corresponds to the green box in **c**. Cell colours are as in **a**–**c**, with cells in blue belonging to regions of higher cell concentration than cells in red. (**e**) The patch concentration enhancement factor, Q, measures the concentration of the most aggregated fraction f of cells relative to that of a non-motile (random) distribution, revealing that motility can drive the formation of patches with concentrations orders of magnitude larger than that of non-motile cells. (**f**) The cell concentration within patches, Q (here for the 10% most aggregated cells, $f = 0.1$), increases with the non-dimensional swimming speed, Φ, and peaks at intermediate stability numbers, $\Psi \sim 1$. The white line denotes the [Ψ, Φ] parameter space inhabited by a species with $B = 5$ s and $V = 1{,}000\ \mu\mathrm{m\,s}^{-1}$ swimming in a turbulent flow with $\varepsilon = 10^{-6}$ (pink square) and 10^{-9} (pink triangle) $\mathrm{m}^2\,\mathrm{s}^{-3}$, and circular markers indicate 10-fold changes in ε. Black circles and open squares are [Ψ, Φ] values at which simulations were performed. Open squares correspond to essentially random distributions ($Q < 0.01$).

the shear from small scales where fluid viscosity dissipates energy. The characteristic size and shear rate of these dissipative scales are proportional to the Kolmogorov length scale, $\eta_K = (\nu^3/\varepsilon)^{1/4} \sim 0.1$–10 mm, and Kolmogorov shear rate, $\omega_K = (\varepsilon/\nu)^{1/2} \sim 0.01$–$10\,\mathrm{s}^{-1}$, respectively, where ν is the kinematic viscosity of seawater and ε the rate at which turbulent energy is dissipated[23–25]. Two dimensionless parameters then control the cells' fate: the swimming number, $\Phi = V_C/V_K$, measuring the swimming speed V_C relative to characteristic small-scale fluid velocities $V_K = \eta_K \omega_K = (\nu\varepsilon)^{1/4}$ (the Kolmogorov velocity), and the stability number, $\Psi = B\omega_K$, measuring how unstable upward swimming cells are to overturning by shear. We note that while most turbulent energy is dissipated by fluid motion with length scales larger than η_K (ref. 23) the Kolmogorov scales remain the appropriate parameters for dimensionless analysis (Supplementary Fig. S8; Supplementary Methods).

Through coupling with turbulence, motility can increase local cell concentrations by one or more orders of magnitude. To quantify local cell concentrations, we used a three-dimensional Voronoi tessellation[26] (Fig. 2d; Supplementary Methods). The fraction f of cells having the largest local concentration were defined as patches and used to compute the patch concentration enhancement factor, $Q = (C—C_P)/C_M$, where C is the mean cell concentration within patches, C_P is its counterpart for a random (that is, non-motile) distribution of cells (which also harbours fluctuations in cell concentration), and C_M is the overall cell concentration. Thus, Q is a dimensionless measure of the increase in the local cell concentration due to motility. We found that motility can profoundly affect patch intensity. For example, the 10% most aggregated motile cells ($f = 0.1$) for $\Psi = 1$ and $\Phi = 2.68$ were nearly 10 times ($Q = 8$) more concentrated than the 10% most aggregated non-motile cells (Fig. 2e). For the 1% most aggregated cells ($f = 0.01$), the enhancement is >50-fold ($Q = 51$). As patches are continuously born by motility and killed by turbulent dispersion, each cell transiently samples regions with high concentrations of conspecifics, on average spending a fraction of time f in regions where the local concentration is Q-fold larger than that of a random distribution.

The patchiness intensity depends on both phytoplankton physiology and environmental conditions. Fast swimming cells (large Φ) with intermediate stability ($\Psi \sim 1$) form the most concentrated patches (Fig. 2f). Owing to the incompressibility of the fluid, cells can form patches only if they swim across streamlines to converge within specific regions of the flow: they do so most effectively when their speed is large and their stabilizing torque strikes a balance between producing a swimming direction that is highly unstable and isotropic ($\Psi \gg 1$) and one that is very stable and uniformly upwards ($\Psi \ll 1$; Supplementary Fig. S9)[22].

Motility-driven unmixing generates strong patchiness for conditions that commonly occur in the ocean. The reorientation timescale, while known only for a handful of species[16,20,21,27–29], generally spans the range $B \sim 1$–10 s, which, for typical turbulent dissipation rates ($\varepsilon = 10^{-8}$–$10^{-6}\,\mathrm{m}^2\,\mathrm{s}^{-3}$), corresponds to $\Psi \sim 1$. Phytoplankton swimming speeds[30,31], $V_C \sim 100$–$1{,}000\,\mu\mathrm{m\,s}^{-1}$, are often comparable to or larger than the Kolmogorov velocities, $V_K \sim 300$–$1{,}000\,\mu\mathrm{m\,s}^{-1}$, associated with these dissipation rates, suggesting Φ can often be of order unity. Thus, we expect that phytoplankton routinely inhabit regions of the $[\Psi, \Phi]$ parameter space where patchiness is intense (Fig. 2f). Importantly, our results indicate that phytoplankton do not need to swim faster than the speed of large-scale turbulent fluctuations to defy the homogenizing effect of turbulent dispersion, as previously suggested[10], they only need to swim at speeds comparable to Kolmogorov fluctuations.

Which feature of turbulence is responsible for patchiness? In contrast to steady vortical flow, where multiple mechanisms produce patches[15], in turbulent flow we found a consistent, strong correlation between cell location and downward flow velocity (Fig. 3d), suggesting that patchiness results from a dominant mechanism: cell focusing in local downwelling regions. This result generalizes previous observations of gyrotactic focusing in laminar downwelling flows[21] and is rationalized by a theoretical analysis of the compressibility of the cell velocity field $\mathbf{v} = \mathbf{u} + \Phi\mathbf{p}$ (the superposition of flow velocity, $\mathbf{u}$, and swimming velocity, $\Phi\mathbf{p}$, where $\mathbf{p}$ is the swimming direction and all velocities are non-dimensionalized by V_K). As $\mathbf{v}$ has non-vanishing divergence, $\nabla \cdot \mathbf{v} = \Phi \nabla \cdot \mathbf{p} = -\Psi\Phi\nabla^2 u_z$ (for $\Psi \ll 1$; where u_z is the vertical component of $\mathbf{u}$; Methods), patches form ($\nabla \cdot \mathbf{v} < 0$) where $\nabla^2 u_z > 0$, or equivalently in downwelling flow ($u_z < 0$), because $\nabla^2 u_z$ and u_z are negatively correlated (Supplementary Fig. S7; Methods). Both of these predictions are in good agreement with simulations (Fig. 3d; Supplementary Fig. S6), suggesting our analytical results offer a rational, mechanistic framework to interpret how motile phytoplankton form patches in disordered flows.

Motility substantially decreases the distance between neighbouring phytoplankton cells, altering the topology of their distribution. We found that the probability $p(r)$ that a pair of cells reside less than a distance r from each other is enhanced for $r < 10\eta_K$ and this enhancement is >100-fold for $r < 0.2\eta_K$ (for $\Psi = 0.68$, $\Phi = 3$; Fig. 3a). For $\varepsilon = 10^{-6}\,\mathrm{m}^2\,\mathrm{s}^{-3}$ ($\eta_K \sim 1$ mm), this translates to a >100-fold increase in the probability that a conspecific resides within $\sim 200\,\mu\mathrm{m}$ of a given cell. Whereas non-motile cells are randomly distributed in three-dimensional space, with $p(r) \sim r^3$, for motile cells we found that $p(r) \sim r^D$ with $D < 3$ (Fig. 3a,b), signifying that the cell distribution is not volume-filling, but instead occupies a lower-dimensional fractal set[32]. Fractal clustering of particles in fluids is well known, for example in particles floating on fluid surfaces[33] and water droplets in clouds[34], and arises as a consequence of an effective compressibility, which here stems from the ability of cells to swim across streamlines. Our analysis of the divergence of $\mathbf{v}$ correctly predicts the patchiness topology: weakly compressible flows are expected to produce particle distributions residing on a fractal set of codimension $D = 3 - a(\Psi\Phi)^2$, where a is a constant and $\Psi \ll 1$ (Methods and Falkovich *et al.*[34]). This relation successfully captured the behaviour of the fractal dimension D computed from simulations for $\Psi < 1$ (Fig. 3c), confirming that the interaction of motility and turbulent flow results in an effective compressibility, which generates patchiness.

Discussion

Patchiness generated by motility-driven unmixing may have a multitude of consequences for phytoplankton. On the one hand, patchiness may be advantageous during times of sexual reproduction, as it reduces distances between conspecific cells and could increase the local concentration of phytoplankton-exuded toxins that stifle competitors[35]. On the other hand, patchiness could be detrimental because it sharpens competition for nutrients[36] and enhances grazing by zooplankton[37,38], whose finely tuned foraging strategies allow them to retain their position within centimeter-scale prey patches[2]. The interaction of motility and turbulence could thus be an important determinant of the relative success of different phytoplankton species and provide a mechanistic basis to help decipher the powerful role turbulence is known to exert on plankton community composition[39].

Unlike passive mechanisms that generate patchiness, such as turbulent stirring, motility-driven unmixing stems from active cell behaviour, opening the intriguing possibility that phytoplankton could regulate their small-scale spatial distribution by adaptively adjusting their position in $[\Psi, \Phi]$ space (Fig. 2f).

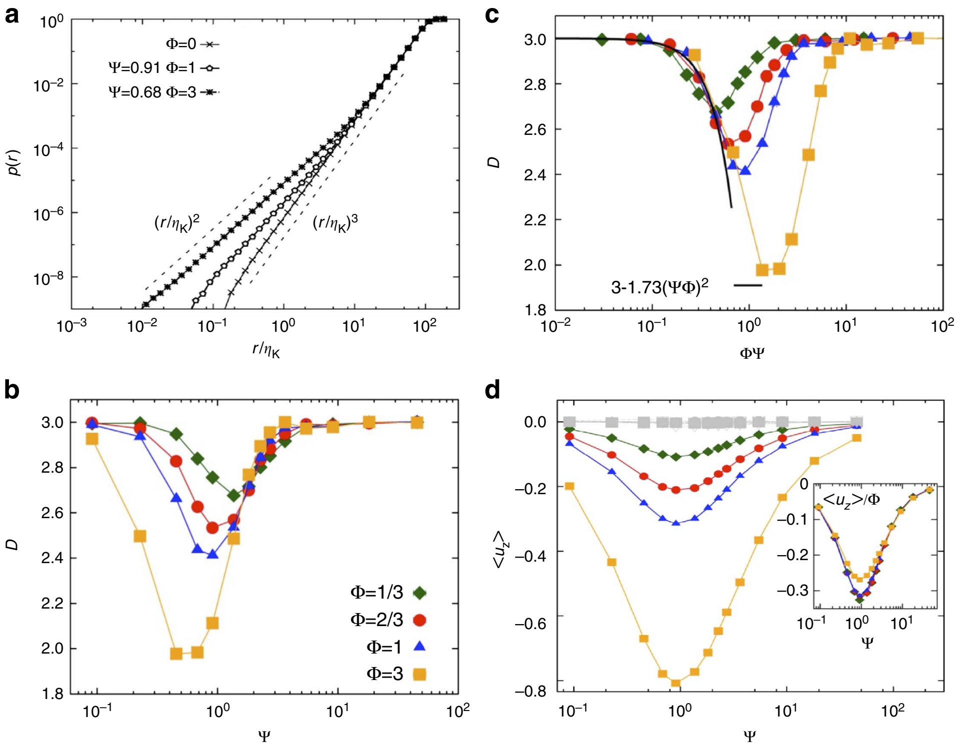

Figure 3 | Gyrotactic cells in a DNS of turbulence. Gyrotactic cells collect in downwelling regions, reducing the distance between neighbouring cells and triggering fractal patchiness. (**a**) Probability $p(r)$ that two cells reside at a distance less than r from each other. While at large scales ($r > 10\eta_K$) the distribution of both non-motile ($\Phi = 0$) and motile ($\Phi > 0$) cells is volume-filling ($p(r) \sim r^3$), at small scales ($r < 10\eta_K$) motile cells exhibit fractal patchiness ($p(r) \sim r^D$ with $D < 3$). (**b**) The fractal dimension D is smallest, corresponding to strongest patchiness, at intermediate stability numbers ($\Psi \sim 1$) and large swimming speeds (large Φ). (**c**) The theoretical prediction of the fractal dimension, $D = 3 - a(\Psi\Phi)^2$ (Methods), accurately captures the simulation results for $\Psi < 1$ (here, $a = 1.73$ and $r^2 = 0.92$). (**d**) The non-dimensional vertical fluid velocity averaged over the positions of all cells, $<u_z>$, shows that populations with intermediate stability ($\Psi \sim 1$) are more likely to reside in downwelling regions ($<u_z> < 0$, coloured lines). This correlation increases with the swimming number, Φ. For comparison, there is no correlation with horizontal fluid velocities (grey symbols). (**d**, inset) Rescaling $<u_z>$ by Φ reveals that $<u_z>$ can reach $\sim$30% of the swimming speed, reducing rates of upward migration.

Cells could regulate Φ by modulating swimming speed and Ψ by altering flagellar stroke[20], overall shape[40] or chloroplast position[41]. Individuals could then actively increase encounter rates with conspecifics, without need for chemical communication, by swimming faster and tuning stability such that $\Psi \sim 1$, or minimize predation risk by slowing down and avoiding the intermediate stability regime. Regardless of whether this mechanism is adaptive or static, these results suggest that small-scale patchiness is a corollary of vertical phytoplankton migration, and that motility-driven patch formation may thus be as common as the species that migrate through the water column. Future field and laboratory experiments may reveal the tradeoffs of directed motility in a turbulent ocean and how it shapes the fate of those at the bottom of the marine food web.

Methods

Phytoplankton culturing and preparation. *H. akashiwo* was grown by inoculating 2 ml of exponential phase culture into 25 ml of sterile f/2 medium, then incubating at 25 °C under continuous fluorescent illumination (70 μE m^{-2} s^{-1}) for 21 days. The culture used in experiments was prepared by diluting 75 ml of the 21-day old culture with 500 ml of f/2 media to achieve a final cell concentration of $\sim 2.5 \times 10^4$ cells ml^{-1}. This concentration strikes a balance between maximizing the number of cells within the central plane (Fig. 1a, green box) and avoiding the bioconvective instabilities that arise when cell concentration exceeds a critical threshold[21]. In control experiments (Supplementary Fig. S2), cells were killed using ethanol (10% v/v) before their introduction into the device.

Experimental vortex apparatus. Two counter-rotating vortices were generated within a custom-made transparent acrylic device (Fig. 1a and Supplementary Fig. S1). A 0.3 ml s^{-1} flow of a *H. akashiwo* culture was driven through each of the two vertical channels of the device using a syringe pump (Harvard Apparatus, PHD 2000) loaded with two syringes (Monoject, 140 ml). A random distribution of cells was initialized within the central cavity of the device (Fig. 1a, green box) by clamping one of the two flexible tubes (Cole Parmer C-Flex, ID 3 mm) that convey flow to the device, which induced a unidirectional flow through the central cavity. Once the tube was unclamped, vortical flow was restored and the experiment began.

A laser sheet, generated using a continuous wave 8 mW Helium-Neon laser (Uniphase, model 1105 P) and a plano-concave cylindrical lens (Thorlabs, 20 mm focal length), illuminated cells along a 1.6-mm thick central plane (-0.8 mm $< y^* < 0.8$ mm, where the asterisk denotes a dimensional variable) where the flow was nearly two-dimensional due to symmetry. All images were captured at 20 Hz with a CCD (charge-coupled device) camera (PCO 1600, Cooke) attached to a dissecting microscope (SMZ1000, Nikon).

Simulations of gyrotaxis within the experimental flow field. To model the flow within the experimental device, we solved the three-dimensional Navier-Stokes equations with the finite element software COMSOL Multiphysics (Burlington, MA), using the experimental device's exact geometry and imposed flow rates. Gyrotactic motility was modelled by integrating the equation for the evolution of the swimming direction of a bottom-heavy spherical cell[21]

$$\frac{d\mathbf{p}}{dt^*} = \frac{1}{2B}[\mathbf{k} - (\mathbf{k}\cdot\mathbf{p})\mathbf{p}] + \frac{1}{2}(\boldsymbol{\omega}^* \times \mathbf{p}) \qquad (1)$$

where $\mathbf{p}$ is the unit vector along the swimming direction, $\boldsymbol{\omega}^* = \boldsymbol{\nabla}^* \times \mathbf{u}^*$ is the fluid vorticity, t^* is time, $\mathbf{k} = [0,0,1]$ is a unit vector in the vertical upwards ($+z^*$) direction, and B is the gyrotactic reorientation timescale, the characteristic time a perturbed cell takes to return to vertical if $\boldsymbol{\omega}^* = 0$. The first term on the right hand side describes the tendency of a cell to remain aligned along the vertical direction due to bottom-heaviness, while the second term captures the tendency of vorticity to overturn a cell by imposing a viscous torque on it. We neglect the effect of cells on the flow. The cell position, $\mathbf{X}^* = (x^*, y^*, z^*)$, was computed by integrating the velocity resulting from the superposition of the swimming velocity, $V_C\,\mathbf{p}$, and the flow velocity, $\mathbf{u}^*$:

$$\frac{d\mathbf{X}^*}{dt^*} = V_C\mathbf{p} + \mathbf{u}^*(\mathbf{X}^*). \tag{2}$$

Cell positions and swimming directions were initialized at random locations within the device and randomly on a unit sphere, respectively. Reflective boundary conditions were applied at all solid boundaries. The swimming speed, V_C, of each cell was drawn from a probability distribution obtained from *H. akashiwo* cells swimming within the central plane of the experimental device in the absence of flow. Cell trajectories were obtained from movies recorded at 20 Hz using automated software (PredictiveTracker; Ouellette *et al.*[42]). To estimate the three-dimensional swimming velocity from its measured (x^*, z^*) projection, we assumed isotropy in x^* and y^* to obtain $V_C = (2{v_x^*}^2 + {v_z^*}^2)^{1/2}$ where v_x^* and v_z^* are the instantaneous cell swimming speeds in the x^* and z^* direction, respectively. The resulting probability density for the cell swimming speed has a mean of 75 µm s^{-1} (Supplementary Fig. S3). All 70,000 cells used in the simulation had a gyrotactic reorientation parameter of $B = 2$ s, based on a previous estimate for *H. akashiwo*[27].

Simulations of gyrotaxis within isotropic turbulence. We solved the three-dimensional Navier-Stokes equations in a fully periodic cubic domain of size $L_B = 2\pi$ with M mesh points using a pseudo-spectral method with a vector potential representation to ensure fluid incompressibility[43]. To eliminate aliasing errors, we used the 2/3 dealiasing technique, which sets the largest 1/3 of all wave numbers to zero after each computation of the nonlinear terms in the Navier-Stokes equation[44], such that the largest resolved wavenumber is $k_{\max} = (1/3)M^{1/3}$. Statistically stationary turbulence was sustained by applying homogeneous, isotropic, time-uncorrelated Gaussian forcing over a narrow shell of small wavenumbers[45], which produces integral-scale fluid fluctuations (that is, the size L of the largest eddy) on the order of the domain size.

Once the velocity field had reached a statistical steady state, gyrotactic cells were initialized with random position in the domain and with orientations randomly distributed over the unit sphere. We seeded the simulation box with 300,000–3,200,000 cells depending on the Taylor Reynolds number Re_λ (Supplementary Table S1; Supplementary Methods). Cell trajectories were integrated using the non-dimensional form of equations 1 and 2,

$$\frac{d\mathbf{p}}{dt} = \frac{1}{2\Psi}[\mathbf{k} - (\mathbf{k}\cdot\mathbf{p})\mathbf{p}] + \frac{1}{2}(\boldsymbol{\omega}\times\mathbf{p}), \tag{3}$$

$$\frac{d\mathbf{X}}{dt} = \Phi\mathbf{p} + \mathbf{u}(\mathbf{X}), \tag{4}$$

where time was non-dimensionalized by $1/\omega_K$, lengths by the Kolmogorov length scale η_K and velocities by the Kolmogorov velocity $V_K = \omega_K\eta_K$. Dimensionless parameters are $\Phi = V_C/V_K$ and $\Psi = B\omega_K$ (ω_K is the Kolmogorov vorticity scale). At each time step of the simulation, the local fluid flow properties ($\boldsymbol{\omega}$ and $\mathbf{u}$) at the particle locations were calculated using a tri-linear interpolation from the computational mesh points.

Previous studies have demonstrated that the trajectories of passive tracer particles integrated via this numerical scheme accurately capture both the velocity[46] and the acceleration[47] statistics of the underlying DNS-derived flow. Moreover, previous studies on clustering of inertial particles[48] have demonstrated the efficacy of this method to resolve sub-Kolmogorov scale fractal aggregations, which we also observed for gyrotactic swimmers.

All analyses were performed after cells had reached a statistically steady distribution, which requires $\sim$30–50 Kolmogorov time scales ($1/\omega_K$), corresponding in our simulations to 1–2 integral time scales (the characteristic timescale of the largest eddies in the flow).

Theoretical prediction of accumulation in downwelling regions. In general, the cell velocity field, $\mathbf{v} = \mathbf{u} + \Phi\mathbf{p}$, and its divergence, $\boldsymbol{\nabla}\cdot\mathbf{v}$, depend on the history of the trajectory of individual cells and can only be calculated statistically. However, in the limit of a large stabilizing torque ($\Psi \ll 1$) the cell orientation quickly reaches equilibrium with the local fluid vorticity, such that $\mathbf{v}$ can be directly calculated using the instantaneous flow field. Assuming $\Psi \ll 1$, the solution to equation 3 is

$$\mathbf{p} \approx (\Psi\omega_y,\ -\Psi\omega_x,\ 1), \tag{5}$$

to leading order in Ψ. This predicts that cells swim upwards with a deviation proportional to Ψ from the vertical. Imposing the incompressibility of the flow ($\boldsymbol{\nabla}\cdot\mathbf{u} = 0$) and applying the definition of vorticity, substitution of equation 5 into equation 4 yields

$$\boldsymbol{\nabla}\cdot\mathbf{v} = -\Psi\Phi\nabla^2 u_z, \tag{6}$$

where u_z is the vertical component of fluid velocity, normalized by the Kolmogorov velocity, V_K. Equation 6 predicts that the cell velocity is compressible and that aggregations form in regions where $\nabla^2 u_z > 0$. This prediction was confirmed in the DNS simulations by calculating $\langle\nabla^2 u_z\rangle$, defined as the mean of $\nabla^2 u_z$ at the position of the cells (Supplementary Fig. S6). We found that $\langle\nabla^2 u_z\rangle$ reaches a maximum for $\Psi \sim 1$ and increases monotonically with Φ, which mirrors the dependence of the aggregation intensity on Ψ and Φ (Figs 2f and 3b; Supplementary Fig. S6), indicating that cells form patches in regions where $\langle\nabla^2 u_z\rangle$ is large.

The prediction that cells collect where $\nabla^2 u_z > 0$ generalizes prior observations that gyrotactic cells tend to collect in downwelling flows[21], because regions of the flow where $\nabla^2 u_z > 0$ tend be highly correlated with regions of downwelling ($u_z < 0$). This correlation can be demonstrated either by analysing the results from the DNS (Supplementary Fig. S7) or via theoretical analysis. The latter is briefly outlined here. By recasting the Navier-Stokes equations as an energy balance one can write[25]

$$-\varepsilon = -\nu\langle|\boldsymbol{\nabla}\mathbf{u}|^2\rangle = \nu\langle\mathbf{u}\cdot\nabla^2\mathbf{u}\rangle = 3\nu\langle u_z\nabla^2 u_z\rangle, \tag{7}$$

where all variables are dimensional (asterisks omitted for brevity), ε is the average energy dissipation rate and the last equality assumes isotropic flow. We can then rewrite the averaged quantity in the last term as:

$$\langle u_z\nabla^2 u_z\rangle = \int_{-\infty}^{\infty} du\, u\langle\nabla^2 u_z|u_z = u\rangle P(u), \tag{8}$$

where $\langle\nabla^2 u_z|u_z = u\rangle$ is a conditional average and $P(u)$ is the probability density distribution of a single component of the flow velocity field at a fixed point, which for turbulent flows is well approximated by the following Gaussian distribution[25]:

$$P(u) = \frac{1}{\sqrt{2\pi u_{\mathrm{rms}}^2}}\exp\left[-\frac{u^2}{2u_{\mathrm{rms}}^2}\right]. \tag{9}$$

Using a closure theory that assumes homogeneous, isotropic turbulent flow[49], the conditional average in equation 8 can be approximated, to leading order, as

$$\langle\nabla^2 u_z|u_z = u\rangle \approx -\frac{\varepsilon}{3\nu u_{\mathrm{rms}}^2}u. \tag{10}$$

Equation 10 is obtained by using a linear approximation for the conditional average and substituting equation 9 into equation 8 and the result into equation 7 (ref. 49). The relation in equation 10, which shows good agreement with our simulations (Supplementary Fig. S7) predicts that, on average, regions with positive $\nabla^2 u_z$ are correlated with downwelling flow ($u_z < 0$), and vice versa.

These two predictions, that is, that cells collect where $\nabla^2 u_z > 0$ and that $\nabla^2 u_z \sim -u_z$, taken together, indicate that an effective compressibility in the cell velocity field (produced by the cells' motility) results in the formation of patches within downwelling regions, rationalizing the results from the turbulence simulations.

Theoretical prediction of *D*. In the previous section we showed that the cell's velocity field $\mathbf{v}$ has non-vanishing divergence in the limit of a strong stabilizing torque ($\Psi \ll 1$). In this limit, cells behave as passive tracers transported by a weakly compressible flow, $\mathbf{v} = \mathbf{u} + \delta\mathbf{w}$ with $\boldsymbol{\nabla}\cdot\mathbf{w} = -\nabla^2 u_z$ and $\delta = \Psi\Phi$ (equation 6). It has been previously shown that tracers in weakly compressible flows ($\delta \ll 1$) tend to form transient clusters of fractal codimension $(3 - D) \propto \delta^2$ (refs 34,50–52). Thus for gyrotactic swimmers with $\Psi \ll 1$, the fractal dimension is predicted as

$$D = 3 - a(\Psi\Phi)^2, \tag{11}$$

where a is a constant that depends on the flow. This result is in good agreement with our simulations for $\Psi < 1$ (Fig. 3c).

References

1. Uda, M. Researches on 'Siome' or current rip in the seas and oceans. *Geophys. Mag.* **11,** 307–372 (1938).
2. Tiselius, P. Behavior of *Acartia tonsa* in patchy food environments. *Limnol. Oceanogr.* **37,** 1640–1651 (1992).
3. Richerson, P., Armstrong, R. & Goldman, C. R. Contemporaneous disequilibrium, a new hypothesis to explain the 'Paradox of the plankton'. *Proc. Natl Acad. Sci. USA* **67,** 1710–1714 (1970).
4. Lasker, R. Field criteria for survival of anchovy larvae - relation between inshore chlorophyll maximum layers and successful 1st feeding. *Fish. Bull.* **73,** 453–462 (1975).
5. Steele, J. H. Spatial heterogeneity and population stability. *Nature* **248,** 83 (1974).
6. Denman, K. L. & Platt, T. The variance spectrum of phytoplankton in a turbulent ocean. *J. Mar. Res.* **34,** 593–601 (1976).
7. Martin, A. P. Phytoplankton patchiness: the role of lateral stirring and mixing. *Prog. Oceanogr.* **57,** 125–174 (2003).
8. Yamazaki, H., Mitchell, J. G., Seuront, L., Wolk, F. & Li, H. Phytoplankton microstructure in fully developed oceanic turbulence. *Geophys. Res. Lett.* **33,** L01603 (2006).
9. Mitchell, J. G., Yamazaki, H., Seuront, L., Wolk, F. & Li, H. Phytoplankton patch patterns: seascape anatomy in a turbulent ocean. *J. Mar. Syst.* **69,** 247–253 (2008).
10. Gallager, S. M., Yamazaki, H. & Davis, C. S. Contribution of fine-scale vertical structure and swimming behavior to formation of plankton layers on Georges Bank. *Mar. Ecol. Prog. Ser.* **267,** 27–43 (2004).

11. Malkiel, E., Alquaddoomi, O. & Katz, J. Measurements of plankton distribution in the ocean using submersible holography. *Meas. Sci. Technol.* **10,** 1142–1152 (1999).
12. Mouritsen, L. T. & Richardson, K. Vertical microscale patchiness in nano- and microplankton distributions in a stratified estuary. *J. Plankton Res.* **25,** 783–797 (2003).
13. Maxey, M. R. & Corrsin, S. Gravitational settling of aerosol particles in randomly oriented cellular flow fields. *J. Atmos. Sci.* **43,** 1112–1134 (1986).
14. Mitchell, J. G., Okubo, A. & Fuhrman, J. A. Gyrotaxis as a new mechanism for generating spatial heterogeneity and migration in microplankton. *Limnol. Oceanogr.* **35,** 123–130 (1990).
15. Durham, W. M., Climent, E. & Stocker, R. Gyrotaxis in a steady vortical flow. *Phys. Rev. Lett.* **106,** 238102 (2011).
16. Kessler, J. O. Hydrodynamic focusing of motile algal cells. *Nature* **313,** 218–220 (1985).
17. Smayda, T. J. Harmful algal blooms: their ecophysiology and general relevance to phytoplankton blooms in the sea. *Limnol. Oceanogr.* **42,** 1137–1153 (1997).
18. Bollens, S. M., Rollwagen-Bollens, G., Quenette, J. A. & Bochdansky, A. B. Cascading migrations and implications for vertical fluxes in pelagic ecosystems. *J. Plankton Res.* **33,** 349–355 (2011).
19. Ryan, J. P., McManus, M. A. & Sullivan, J. M. Interacting physical, chemical and biological forcing of phytoplankton thin-layer variability in Monterey Bay, California. *Cont. Shelf Res.* **30,** 7–16 (2010).
20. O'Malley, S. & Bees, M. A. The orientation of swimming biflagellates in shear flows. *Bull. Math. Biol.* **74,** 232–255 (2012).
21. Pedley, T. J. & Kessler, J. O. Hydrodynamic phenomena in suspensions of swimming microorganisms. *Annu. Rev. Fluid Mech.* **24,** 313–358 (1992).
22. Lewis, D. M. The orientation of gyrotactic spheroidal micro-organisms in a homogeneous isotropic turbulent flow. *Philos. Tr. R. Soc. S.-A* **459,** 1293–1323 (2003).
23. Jumars, P. A., Trowbridge, J. H., Boss, E. & Karp-Boss, L. Turbulence-plankton interactions: a new cartoon. *Mar. Ecol. Evol. Persp.* **30,** 133–150 (2009).
24. Thorpe, S. A. *An Introduction to Ocean Turbulence* (Cambridge University, 2007).
25. Frisch, U. *Turbulence: the Legacy of A. N. Kolmogorov* (Cambridge University, 1995).
26. Rycroft, C. H. Voro++: A three-dimensional Voronoi cell library in C++. *Chaos* **19,** 04111 (2009).
27. Durham, W. M., Kessler, J. O. & Stocker, R. Disruption of vertical motility by shear triggers formation of thin phytoplankton layers. *Science* **323,** 1067–1070 (2009).
28. Drescher, K. *et al.* Dancing *Volvox*: hydrodynamic bound states of swimming algae. *Phys. Rev. Lett.* **102,** 168101 (2009).
29. Hill, N. A. & Häder, D. P. A biased random walk model for the trajectories of swimming micro-organisms. *J. Theor. Biol.* **186,** 503–526 (1997).
30. Fauchot, J., Levasseur, M. & Roy, S. Daytime and nighttime vertical migrations of *Alexandrium tamarense* in the St. Lawrence estuary (Canada). *Mar. Ecol. Prog. Ser.* **296,** 241–250 (2005).
31. Kamykowski, D., Reed, R. E. & Kirkpatrick, G. J. Comparison of sinking velocity, swimming velocity, rotation, and path characteristics among six marine dinoflagellate species. *Mar. Biol.* **113,** 319–328 (1992).
32. Grassberger, P. & Procaccia, I. Measuring the strangeness of strange attractors. *Physica D.* **9,** 189–208 (1983).
33. Sommerer, J. C. & Ott, E. Particles floating on a moving fluid - a dynamically comprehensible physical fractal. *Science* **259,** 335–339 (1993).
34. Falkovich, G., Fouxon, A. & Stepanov, M. G. Acceleration of rain initiation by cloud turbulence. *Nature* **419,** 151–154 (2002).
35. Legrand, C., Rengefors, K., Fistarol, G. O. & Granéli, E. Allelopathy in phytoplankton - biochemical, ecological and evolutionary aspects. *Phycologia* **42,** 406–419 (2003).
36. Siegel, D. A. Resource competition in a discrete environment: Why are plankton distributions paradoxical? *Limnol. Oceanogr.* **43,** 1133–1146 (1998).
37. Grünbaum, D. Predicting availability to consumers of spatially and temporally variable resources. *Hydrobiologia* **480,** 175–191 (2002).
38. Tiselius, P., Jonsson, P. R. & Verity, P. G. A model evaluation of the impact of food patchiness on foraging strategy and predation risk in zooplankton. *Bull. Mar. Sci.* **53,** 247–264 (1993).
39. Margalef, R. Life-forms of phytoplankton as survival alternatives in an unstable environment. *Oceanol. Acta* **1,** 493–509 (1978).
40. Zirbel, M. J., Veron, F. & Latz, M. I. The reversible effect of flow on the morphology of *Ceratocorys horrida* (Peridiniales, Dinophyta). *J. Phycol.* **36,** 46–58 (2000).
41. Swift, E. & Taylor, W. R. Bioluminescence and chloroplast movement in the dinoflagellate *Pyrocystis lunula*. *J. Phycol.* **3,** 77–81 (1967).
42. Ouellette, N. T., Xu, H. T. & Bodenschatz, E. A quantitative study of three-dimensional Lagrangian particle tracking algorithms. *Exp. Fluids* **40,** 301–313 (2006).
43. Canuto, C. *Spectral Methods in Fluid Dynamics* (Springer, 1988).
44. Orszag, S. On the elimination of aliasing in finite-difference schemes by filtering high-wavenumber components. *J. Atmos. Sci.* **28,** 1074 (1971).
45. Eswaran, V. & Pope, S. B. An examination of forcing in direct numerical simulations of turbulence. *Comput. Fluids* **16,** 257–278 (1988).
46. Arneodo, A. *et al.* Universal intermittent properties of particle trajectories in highly turbulent flows. *Phys. Rev. Lett.* **100,** 254504 (2008).
47. Biferale, L. *et al.* Multifractal statistics of Lagrangian velocity and acceleration in turbulence. *Phys. Rev. Lett.* **93,** 064502 (2004).
48. Bec, J. *et al.* Heavy particle concentration in turbulence at dissipative and inertial scales. *Phys. Rev. Lett.* **98,** 084502 (2007).
49. Wilczek, M., Daitche, A. & Friedrich, R. On the velocity distribution in homogeneous isotropic turbulence: correlations and deviations from Gaussianity. *J. Fluid Mech.* **676,** 191–217 (2011).
50. Falkovich, G., Gawedzki, K. & Vergassola, M. Particles and fields in fluid turbulence. *Rev. Mod. Phys.* **73,** 913–975 (2001).
51. Falkovich, G. & Fouxon, A. Entropy production and extraction in dynamical systems and turbulence. *New J. Phys.* **6,** 50 (2004).
52. Fouxon, I. Distribution of particles and bubbles in turbulence at a small Stokes number. *Phys. Rev. Lett.* **108,** 134502 (2012).

Acknowledgements

We thank David Kulis and Donald Anderson for supplying *H. akashiwo*, Calcul en Midi-Pyrénées and Cineca Supercomputing Center for use of high-performance computational facilities, and Katharine Coyte, Kevin Foster, Nuno Oliveira and Jonas Schluter for comments on the manuscript. We acknowledge the support of the Human Frontier Science Program (to W.M.D.), MIUR PRIN-2009PYYZM5 and EU COST Action MP0806 (to G.B., M.C. and F.D.), MIT MISTI-France program (to E.C. and R.S.), and NSF grants OCE-0744641-CAREER and CBET-1066566 (to R.S.).

Author contributions

W.M.D., M.B. and R.S. were responsible for vortex experiments and simulations thereof, W.M.D., E.C., F.D.L., G.B., M.C. and R.S. performed and analysed DNS simulations, F.D.L., G.B. and M.C. developed analytical tools to interpret DNS simulations, W.M.D. and R.S. wrote the paper with input from all authors.

Additional information

Supplementary information accompanies this paper at http://www.nature.com/naturecommunications

Competing financial interests: The authors declare no competing financial interests.

Reprints and permission information is available online at http://npg.nature.com/reprintsandpermissions/

How to cite this article: Durham W. M. *et al.* Turbulence drives microscale patches of motile phytoplankton. *Nat. Commun.* 4:2148 doi: 10.1038/ncomms3148 (2013)

SUPPLEMENTARY INFORMATION

Supplementary Figures

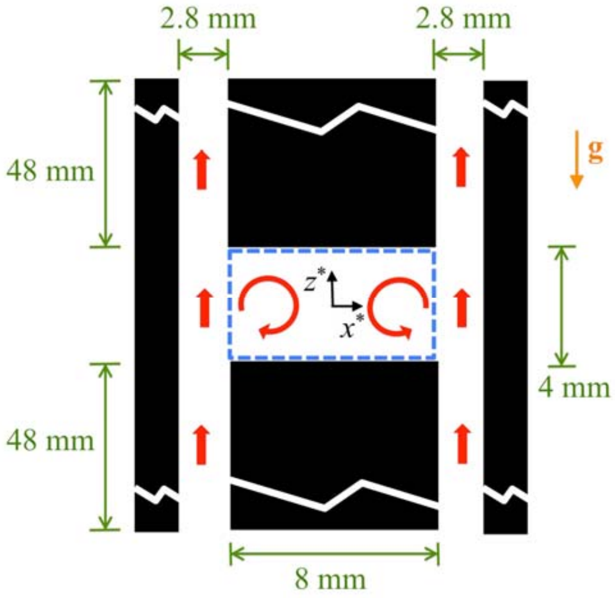

Supplementary Figure S1 | Schematic of the experimental device. The device extends 18 mm in the y^* direction (*i.e.*, into the plane). The central plane is denoted with the dashed blue box. Not drawn to scale.

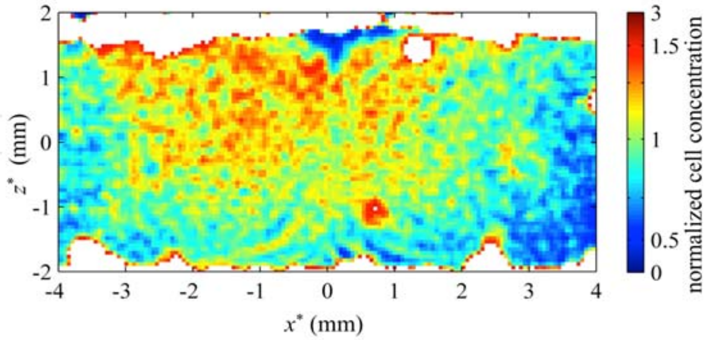

Supplementary Figure S2 | A histogram of cell concentration from experiments using dead cells reveals no aggregations. Cell concentrations were normalized using the same method as in Fig. 1c.

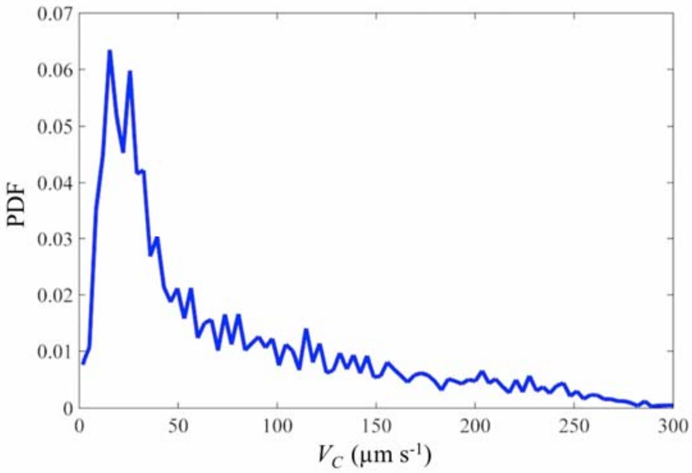

Supplementary Figure S3 | Probability density function of the three-dimensional swimming speed, V_C, of *Heterosigma akashiwo*. The three-dimensional swimming speed was estimated assuming $V_C = (2v_x^{*2} + v_z^{*2})^{1/2}$, where v_x^* and v_z^* are the instantaneous swimming speeds in the *x* and *z* direction, respectively.

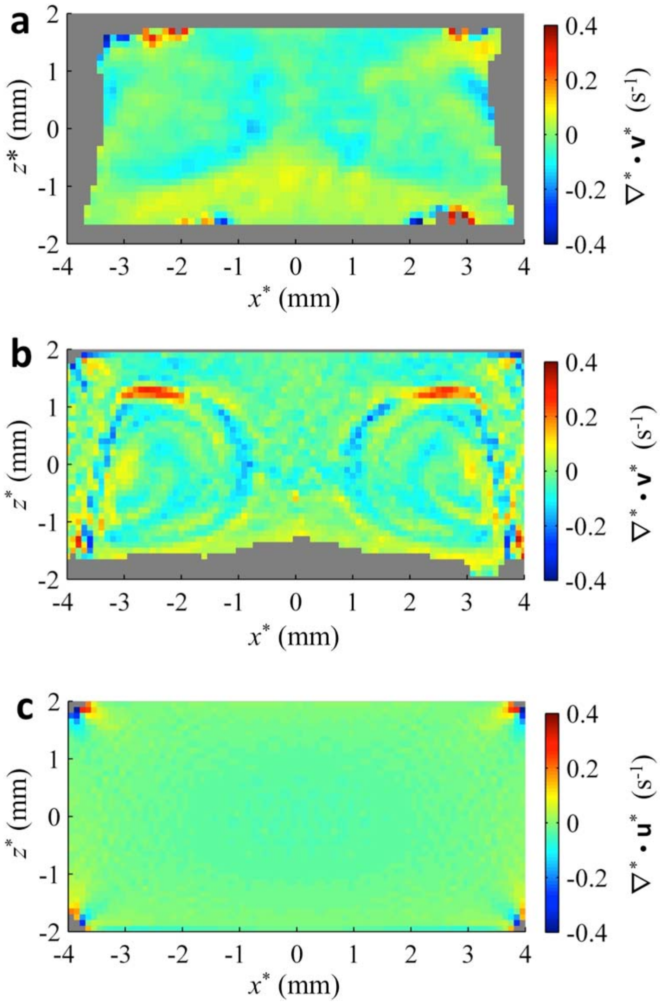

Supplementary Figure S4 | Measurements of divergence. The two-dimensional divergence of the y^*-averaged cell velocity ($\nabla^* \cdot \mathbf{v}^*$) in experiments (a) and from a model that simulates gyrotactic motility within the experimental flow (b) bear strong resemblance to one another, suggesting that the similar accumulation patterns in both (Fig. 1c,d) are borne by the same processes. In contrast, the divergence of the y^*-averaged fluid flow velocity ($\nabla^* \cdot \mathbf{u}^*$) exhibits a divergence of approximately zero within the central plane (c), except within the corner regions where the spatial sampling of the simulated velocity field is not sufficient for accurate differentiation.

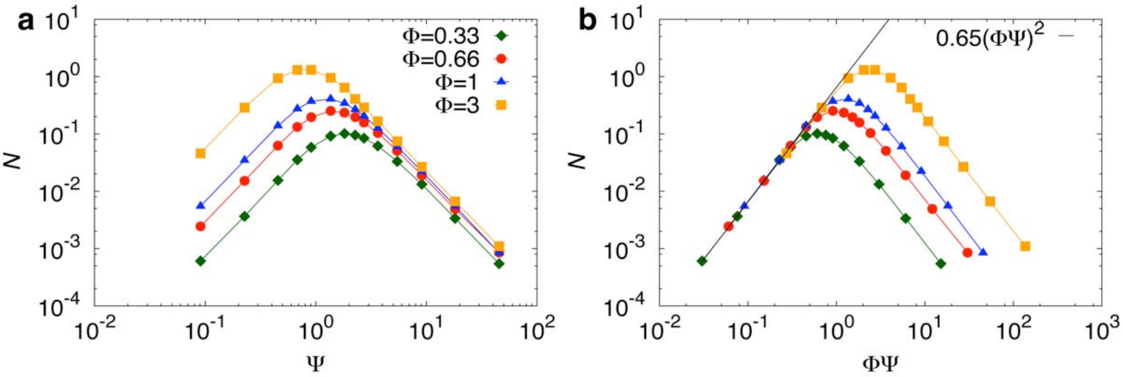

Supplementary Figure S5 | The normalized box probability index, *N*, as a function of (a) the cell stability number, Ψ, and (b) the predicted scaling (see Section 4 of Supplementary Methods). Results obtained using $Re_\lambda = 62$.

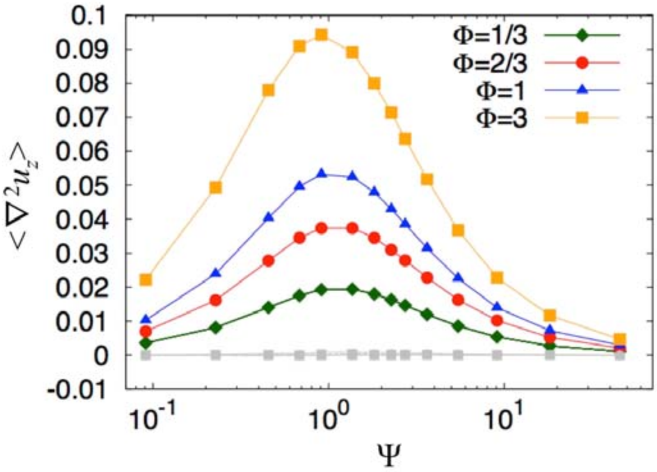

Supplementary Figure S6 | The non-dimensional Laplacian of the vertical component of the velocity of the fluid, $\nabla^2 u_z$, averaged over the position of 300,000 cells, as a function of the stability number Ψ for different swimming numbers Φ. Grey symbols show $<\nabla^2 u_x>$ and $<\nabla^2 u_y>$ for comparison. Results obtained using $Re_\lambda = 62$.

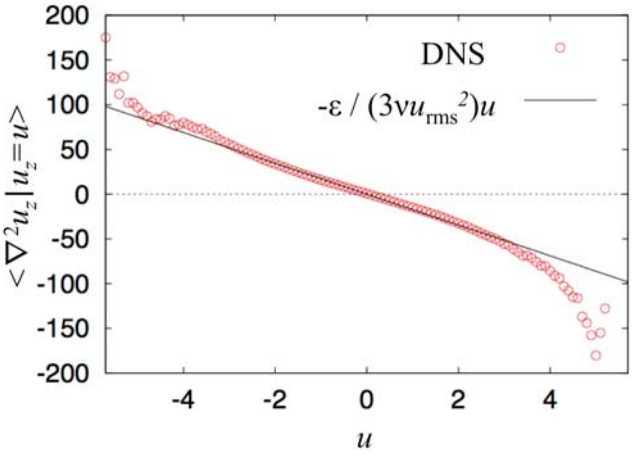

Supplementary Figure S7 | The average of the dimensional Laplacian of the vertical component of the fluid velocity conditioned on the vertical velocity value, $<\nabla^2 u_z | u_z = u>$, as a function of the dimensional local vertical velocity, u (asterisks are omitted for brevity). The straight line shows the theoretical prediction (Eq. 10). The DNS data (red circles) were obtained by sampling the flow ($Re_\lambda = 62$) at random locations in the domain.

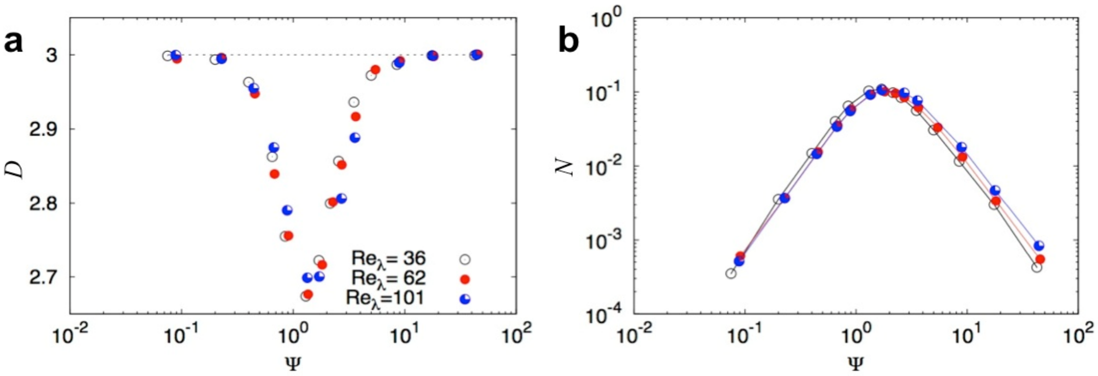

Supplementary Figure S8 | The aggregation intensity is only weakly dependent on the Taylor Reynolds number, Re_λ. The effect of Re_λ on (a) D and (b) N. Regardless of the Re_λ, the maximum level of aggregation occurs at a $\Psi \sim 1$, confirming that cell aggregations originate at the Kolmogorov scale. All results shown are for $\Phi = 1/3$.

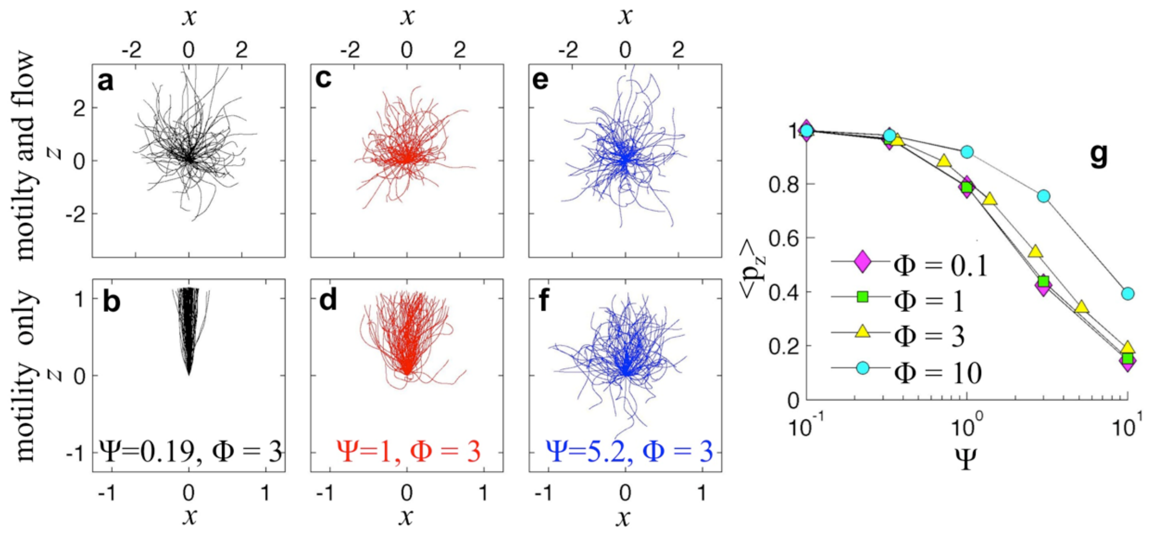

Supplementary Figure S9 | Turbulence can inhibit the vertical migration of phytoplankton. (a-f), The trajectories of 100 cells swimming in a turbulent flow at three different stability numbers, Ψ. Although vertical migration is difficult to discern in the raw trajectories (a,c,e) due to advection by the flow, when the latter is subtracted (b,d,f) it is clear that turbulence progressively hampers vertical migration as Ψ increases. **(g)** The erosion of vertical migration was quantified by the average vertical projection of the swimming direction, $<p_z>$, of 10^5 cells. Very stable cells ($\Psi << 1$) always swim vertically ($<p_z> = 1$), whereas progressively more unstable cells (increasing Ψ) lose the ability to vertically migrate. In addition, vertical migration is favored by large swimming speeds (Φ), as fast swimming cells quickly traverse regions of locally enhanced shear, reducing the time over which they can be be reoriented by flow. Panels a-f each show the two-dimensional projection of trajectories randomly distributed in the flow over 20 Kolmogorov timescales. Trajectories in (a,c,e) show movement due both advection and motility ($d\mathbf{X}/dt = \mathbf{u}(\mathbf{X}) + \Phi\mathbf{p}$), while trajectories in (b,d,f) have been postprocessed to show movement due to motility only ($d\mathbf{X}/dt = \Phi\mathbf{p}$). For visualization purposes the starting point of each trajectory has been translated to the origin. $Re_\lambda = 62$ for all panels.

Supplementary Table

Re_λ	M	Number of cells	λ/η_K
36	64^3	300,000	11.7
62	128^3	300,000	15.7
101	256^3	2,400,000	19.5
123	512^3	3,200,000	21.7

Supplementary Table S1 | Parameters of the direct numerical simulations of turbulence. Re_λ is the Taylor Reynolds number, M is the number of nodes in the computational mesh, and λ/η_K is the Taylor scale normalized by the Kolmogorov scale.

Supplementary Methods

1. Analysis of experimental measurements

Histograms of cell concentration within the region illuminated by the laser sheet (Fig. 1c and Supplementary Fig. S2) were obtained by identifying the (x^*, z^*) positions of the centroids of individual cells over a period of 4.4 min (5,300 images) and 3.8 min (4,540 images) for the swimming and killed cell treatments, respectively. To obtain the normalized cell concentration, the cumulative number of cells residing within 114 μm × 114 μm bins over the entire experimental time was divided by the mean number of cells per bin within the region defined by -4 mm < x^* < 4 mm and -1.6 mm < z^* < 1.6 mm, away from the device's solid boundaries.

To calculate the two-dimensional cell velocity, $\mathbf{v}^* = (v_x^*, v_z^*)$, within the central plane and its in-plane divergence, $\nabla^*\cdot\mathbf{v}^* = \partial v_x^*/\partial x^* + \partial v_z^*/\partial z^*$ (Supplementary Fig. S4a), we reconstructed 3.6×10^5 trajectories of individual cells swimming within the central plane (-4 mm < x^* < 4 mm, -0.8 mm < y^* < 0.8 mm, -2 mm < z^* < 2 mm) over time and space, using automated software (PredictiveTracker, ref. 42). The trajectories had an average length of 0.49 s (9.8 time points). Cell trajectories were used to obtain the Eulerian velocity field by calculating the mean cell velocity within 114 μm × 114 μm bins in (x^*, z^*) space. An average of 1,515 velocity measurements were obtained for each bin. The velocity profile in Fig. 1b was obtained by tracking dead phytoplankton cells.

While the flow velocity, $\mathbf{u}^* = (u_x^*, u_y^*, u_z^*)$, within the device is three-dimensional, by symmetry we predict that $u_y^* = 0$ at every point within the plane, $y^* = 0$, and similarly that u_y^* averaged over a slice that symmetrically spans $y^*=0$, -0.8 mm < y^* < 0.8 mm (*i.e.* the laser illuminated 'central plane'), equals zero. Therefore, the divergence of the y-averaged flow within the central plane is expected to be zero $(\nabla^*\cdot\mathbf{u}^*) = \partial u_x^*/\partial x^* + \partial u_z^*/\partial z^* = 0$, due to the flow's incompressibility. In contrast, the divergence of the cell velocity field in the central plane is non-zero $(\nabla^*\cdot\mathbf{v}^*) = \partial v_x^*/\partial x^* + \partial v_z^*/\partial z^* \neq 0$) and its sign can be used to diagnose regions of the flow where cells converge ($\nabla^*\cdot\mathbf{v}^* < 0$), increasing the local cell concentration, from regions where cells diverge ($\nabla^{*}\cdot\mathbf{v}^{*} > 0$), decreasing the local cell concentration. The divergence field was calculated via numerical differentiation of the velocity field and was smoothed with a two-dimensional Gaussian filter (with standard deviation of 0.1 mm) to reduce noise (Supplementary Fig. S4a).

2. Analysis of simulations of gyrotactic motility within experimental flow field

The histogram of cell concentration for the simulations (Fig. 1d) was computed by sampling the x^{*} and z^{*} positions of the cells in 100 µm × 100 µm bins within the region -1 mm < y^{*} < 1 mm, at intervals of 1 s. The cumulative counts over a simulation period of 2 min were divided by the mean cell concentration in the center region (-4 mm < x^{*} < 4mm and -1.6 mm < z^{*} < 1.6mm) to obtain normalized cell concentrations.

The divergence field for the simulations (Supplementary Fig. S4b) was computed in a manner analogous to what done for the experiments: for trajectories residing in the region of the device defined by -1 mm < y^{*} < 1 mm, the x^{*} and z^{*} velocities were sampled in 100 µm x 100 µm bins. The cell velocity field was constructed using the mean velocity from each bin; the two-dimensional divergence, $\nabla^{*}\cdot\mathbf{v}^{*} = \partial v_x^{*}/\partial x^{*} + \partial v_z^{*}/\partial z^{*}$, was computed from this velocity field using two-dimensional Gaussian filtering (with standard deviation of 0.05 mm) to reduce noise. An average of 386 velocity measurements was recorded in each bin.

The divergence field of the flow within the center plane ($\nabla^{*}\cdot\mathbf{u}^{*} = \partial u_x^{*}/\partial x^{*} + \partial u_z^{*}/\partial z^{*}$, Supplementary Fig. S4c) was obtained by averaging (u_x^{*}, u_z^{*}) over -1 mm < y^{*} < 1 mm and calculating the derivatives numerically without smoothing.

3. Quantification of cell aggregation intensity in DNS simulations

To quantify the patchiness generated the interaction of gyrotactic motility with isotropic turbulence, we used three different aggregation metrics: the patch concentration enhancement factor, *Q* (Fig. 2e,f), the correlation fractal dimension, *D* (Fig. 3b,c; ref. 32), and the normalized box probability index, *N* (Supplementary Figs. S5 and S8b; ref. 53). Three different metrics were used to ensure that conclusions were not sensitive to the particular choice of metric. All three metrics indicate that maximal aggregation intensity occurred at intermediate stability (*i.e.,* $\Psi \sim 1$) and increased monotonically with increasing swimming speed (*i.e.,* increasing Φ).

Calculation of *Q.* Three-dimensional Voronoi tessellations of the particle distributions were obtained using the software Voro++ [26], which accounted for the triply periodic boundaries of the computational volume (the Voronoi tessellation shown in Fig. 2d uses non-periodic boundaries, as only a small segment of the full computational domain is shown). The *Q* value presented for each [Ψ, Φ] pair was computed as the average value from eighteen snapshots of the instantaneous positions of 100,000 cells, each separated in time by at least 10 Kolmogorov timescales.

Calculation of *D.* The probability $p(r)$ (Fig. 3a) was obtained by computing the pairwise Euclidean distance between K = 300,000 cells in each of ≈100 snapshots of the particle distribution, each separated in time by more than 20 Kolmogorov timescales. In each snapshot, $p(r)$ was calculated as $p(r) = g(r)/K^2$, where $g(r)$ is the total number of pairwise distances less than r. Applying the definition $p(r)\sim r^D$, we calculated D as the slope of d(log[$p(r)$])/d(log[r]) for $r/\eta_K \lesssim 1$ using the average $p(r)$ from the snapshots.

<u>Calculation of N</u>. The computational domain was partitioned into boxes of length $\Lambda \approx 3\eta_K$. The number of cells residing in each box, n, was used to obtain the box occupancy function, $f(n)$. While the mean of $f(n)$, $b = \langle n \rangle$, is a constant (equal to the mean cell number density), the standard deviation of $f(n)$, $\sigma = (\langle n^2 \rangle - \langle n \rangle^2)^{1/2}$, depends on the manner in which cells are distributed, with more patchy distributions having larger σ. If cells are randomly distributed throughout the domain, the standard deviation is that of a Poisson distribution, $\sigma_P = b^{1/2}$. To measure the particle distribution's deviation from Poisson, we calculated $N = (\sigma - \sigma_P)/b$ (ref. 53): for $N > 0$, the distribution of cells is more patchy than a random distribution (Supplementary Figs. S5 and S8b). To control for statistical fluctuations, this metric was calculated every 2 Kolmogorov time scales and N was taken as the average over more than 10^3 Kolmogorov time scales.

4. Theoretical prediction of *N*

The theoretical prediction of the fractal dimension D (section 8.2) can be related to the normalized box probability index N (ref. 54). Briefly, with the assumption that cells are randomly (Poisson) distributed over the fractal set of dimension $D < 3$ (and hence not uniformly distributed over the volume), one finds that the box probability $f(n)$ (the probability to have n cells in a box of size Λ) is related to the box probability on the fractal set $f_F(n)$, which is given by a Poisson distribution with mean b_F rescaled as $b_F = b\,(L_B/\Lambda)^{3-D}$, where L_B is the size of the domain.

Similarly, the variance of n, σ^2, can be related to b as[54].

$$\sigma^2 = \langle n^2 \rangle - \langle n \rangle^2 = b\left[1 + b\left(\left(\frac{\Lambda}{L_B}\right)^{D-3} - 1\right)\right]. \qquad \text{(S1)}$$

Applying the definition of N and via a Taylor expansion of D–3, one finds

$$N \approx \frac{(3-D)b^{1/2}}{2}\ln\left(\frac{L_B}{\Lambda}\right). \qquad \text{(S2)}$$

Substitution of Eq. (11) into Eq. (S2) yields the prediction $N \propto (\Phi\Psi)^2$ (for $\Psi \ll 1$), which is in agreement with simulations (Supplementary Fig. S5b).

5. Cell aggregation in flows with variable Taylor Reynolds number, Re$_\lambda$

The range of length scales within a turbulent flow is quantified by the Taylor Reynolds number, $\mathrm{Re}_\lambda = u_{\mathrm{rms}}\lambda/\nu$, where $\lambda = u_{\mathrm{rms}}(15\nu/\varepsilon)^{1/2}$ is the Taylor length scale and u_{rms} is the root mean square fluid velocity. Larger Re_λ correspond to a greater separation between the size of integral-scale fluctuations, L, and the size of Kolmogorov-scale fluctuations, η_K. We calculated turbulent flows for four different Taylor Reynolds numbers, ranging from 36 to 123, by varying the number of mesh points M from 64^3 to 512^3 to ensure that the Kolmogorov scale η_K was fully resolved (i.e. $k_{\max}\eta_K \geq 1$) in each case (Supplementary Table S1). In all simulations, the separation between forcing and dissipation scales was sufficient to produce the universal characteristics of a homogeneous isotropic turbulent flow. Data shown in Figs. 2 and 3 were obtained at $\mathrm{Re}_\lambda = 62$.

We found that the aggregation intensity (as measured by N and D) was only weakly dependent on Re_λ for the parameters we tested (Supplementary Fig. S8), suggesting that motility-driven unmixing can overcome turbulent dispersion in a broad range of natural phytoplankton habitats, from pycnoclines ($\mathrm{Re}_\lambda \approx 20$) to deep chlorophyll maxima ($\mathrm{Re}_\lambda \approx 150$) (refs. 55,56). Furthermore, the finding that maximal aggregation occurs at $\Psi \sim 1$ is robust to changes in Re_λ within the range tested (Supplementary Fig. S8), provides further substantiation that motility-driven unmixing is controlled by the velocity gradients at the Kolmogorov scale.

Supplementary References

53 Fessler, J. R., Kulick, J. D. & Eaton, J. K. Preferential concentration of heavy particles in a turbulent channel flow. *Phys. Fluids* **6**, 3742-3749 (1994).

54 Dubrulle, B. & Lachiéze-Rey, M. The poisson-distribution on a fractal. *Astron. Astrophys.* **287**, 361-367 (1994).

55 Maar, M., Nielsen, T. G., Stips, A. & Visser, A. W. Microscale distribution of zooplankton in relation to turbulent diffusion. *Limnol. Oceanogr.* **48**, 1312-1325 (2003).

56 Tennekes, H. & Lumley, J. L. *A first course in turbulence*. (MIT Press, Cambridge, USA, 1972).